

Feature Article

Building Color Management Modules Using Linear Optimization II. Prepress System for Offset Printing

Koichi Iino* and Roy S. Berns†

Munsell Color Science Laboratory, Chester F. Carlson Center for Imaging Science, Rochester Institute of Technology, 54 Lomb Memorial Drive, Rochester, New York 14623-5604

* Toppan Printing Co., Ltd., Technical Research Institute, Manufacturing Research Laboratory, 4-2-3 Takanaodai-Minami, Sugito-Machi, Kitakatsusika-Gun, Saitama 345-8508, Japan

A spectral model was derived to predict the spectral reflectance factor of colors formed using a color proofing system simulating offset printing. A first-order model was based on the spectral Neugebauer equation modified by the Yule-Nielsen correction in which n was assumed to vary as a function of wavelength. The n_i and effective dot areas were optimized using primary (cyan, magenta, yellow, and black) halftone tints. Systematic errors were observed. The systematic error behaved in a similar fashion to the phenomenon of ink trapping. Because ink trapping, ink spread, ink mixture and variance of mechanical dot gain were negligible for this proofing system, this is an optical effect to be referred to as "optical trapping." An interaction model was derived that compensated for optical trapping. Adding the optical trapping effect to the first-order model significantly improved model prediction to an average ΔE_{ab}^* of 2.2 with a maximum of 5.5. A simple black printer model was derived for an inversion of the forward model that aimed to provide a similar black amount with a conventional color-separation method and colorimetric match applying a concept of under-color removal (UCR) in original density space with tone reproduction curves of a gray scale. Using the Simplex method, the modified spectral Neugebauer model with the black printer model was inverted to build a backward model. Influences of the dot area transform function obtained from the backward model were compared with those from a conventional method for an evaluation of similarity. A desktop drum scanner was colorimetrically characterized using a spectral reconstruction model for a reflective photographic material to build a concatenated device profile in which digital counts of a scanned photographic reflection print were the input and those of the proofing system were the output. Performances of the concatenated device profile were evaluated for practical use. The average ΔE_{ab}^* error from the profile was 2.1 including colors outside of the proofing system's color gamut.

Journal of Imaging Science and Technology 42: 99–114 (1998)

Introduction

Color management modules, or CMMs, are a set of equations or a multi-dimensional color look-up table (CLUT) that facilitate color reproduction among digital color imaging devices such as scanners, displays, and printers. As described¹ in Part I of this two-part article, three steps are required: colorimetric device characterization (i.e., building device profiles), color appearance modeling, and color gamut mapping. Part I was concerned with building and evaluating CMMs for desktop color systems consisting of CCD linear-array scanners and ink-jet printers. Two main conclusions were drawn. First, generating device profiles using analytical models was both accurate and efficient. Small sample sizes and reasonable colorimetric accuracy can facilitate the frequent building of new profiles with changes in consumables. Although this approach was used previously by one of the authors for continuous tone printing,² it was unclear whether an analytical model would result in sufficient accuracy for halftone printing. Second, the Simplex method was an efficient linear optimization method to invert analytical printer forward models. As a direct search method, it did not suffer from the conver-

gence problems near the edge of the printer's color gamut that were encountered using the Newton-Raphson method.

Desktop applications are but one among a growing list of color systems relying on principles of device-independent color and incorporating the use of CMMs to achieve acceptable color reproduction quality. We were particularly interested in extending our research into conventional offset printing. This presented several interesting challenges. The first was developing analytical models for reflection scanning and rotated-screen offset lithography with sufficient colorimetric accuracy for high-quality printing. (Reflection input was used to minimize issues concerned with appearance matching and color gamut mapping between transparencies and prints.) The colorimetric accuracy reported in Part I for desktop applications was insufficient for quality color publications such as glossy magazines and books.

Second, the black printer characteristics of the desktop ink-jet printer used in Part I was predefined and fixed at 100% GCR (gray-component replacement). This resulted in 3 degrees of freedom in both input and output stages of model inversion although the printer is a four-color printer. In offset printing, the black printer characteristics are an adjustable parameter. When color separations are based on colorimetric models, the solution is underdetermined where 3 degrees of freedom exist in the input stage (colorimetric-based coordinates) and 4 degrees of freedom in the output stage (cyan, magenta, yellow, and black ink amounts). Several methods have been described to solve

Original manuscript received April 2, 1997.

† IS&T Member

© 1998, IS&T—The Society for Imaging Science and Technology.

this underdetermined problem. One technique³ was based on an analysis of existing conventional printing separation techniques such as UCR (under-color removal), UCA (under-color addition), and GCR. Unfortunately, this method had insufficient colorimetric accuracy⁴ because the three- to four-color conversion was performed in the dot space directory. As a consequence, colorimetric identity was not guaranteed. Other techniques⁵⁻⁸ have first defined an arbitrary amount of black ink to have a determined solution. However, this results in black ink characteristics that are unconventional.

This leads to the third challenge. It is critical that the black ink characteristics are similar to that achieved in conventional color-separation systems. For example, Toppan developed a system⁹ for in-house use that converted between digital image data and four-color dot-area data based on colorimetry. However, it was reported that the initial version of the system was unacceptable for experienced prepress operators because combinations of each ink amount were quite different from those obtained by a conventional color-separation system. The operators reported two problem areas: difficulty in retouching color in later processes and difficulty in predicting what the color would look like when printed. Clearly, a major hidden requirement for introducing novel systems based on principles of device-independent color into printing production is not to deviate too far from conventional methods or from an operator's experiential understanding. Similar problems were encountered by Schreiber.^{10,11}

A final challenge is modeling offset lithography. It is well known that process control is difficult to maintain under normal operating conditions. Because of the resulting ink-on-paper variance, it would be difficult to separate limitations in model accuracy from printing variance. As a consequence, an industry-accepted proofing system was used to simulate offset lithography.

Thus, Part II of this research is concerned with building and testing CMMs for use in conventional offset printing based on methodologies that address the above challenges.

Experimental

Color Proofing System. A 3M Matchprint III Color Proofing System was used to simulate offset printing. It is assumed that Matchprint does not have mechanical variances caused by ink spread, ink mixture, or ink trapping, but does have a small amount of mechanical dot gain as a result of the transformation process from separation films to pigment films. Thus, the mechanical dot gain is a constant parameter. This facilitates the consideration of only the optical behavior of halftone ink on paper because all observed optical phenomena are separated from mechanical ones. Although it seems that this proofing system would not simulate printing well because of a lack of mechanical dot gain, its widespread use within the industry indicates the contrary. Furthermore, extending a model of Matchprint to actual printing by increasing the derived mechanical effects seems straightforward. This research was performed under the assumption that an accurate model of Matchprint would model most of the significant optical and mechanical behavior of actual printing.

Matchprint samples were made by the usual process. Squared dot and hard dot screens and 175-lpi resolution were selected as screening conditions because these are some of the most common conditions in practical use. A modeling target and a verification target were made from four-color digital data using Adobe Photoshop 3.0 and the layout of the digital data was made by Quark Express 3.3.

These digital data were ripped by a Scitex PS2 image setter. Separation films were made from these ripped data on a Scitex Doleve 400.

Input Device. A Howtek Scanmaster D4000 reflection and transmission scanner was used as the input device. This is a rotating drum, three-filter photomultiplier tube scanner capable of 50- to 4000-dpi spatial resolution. Two tungsten halogen reflector lamps were incorporated as light sources. The scanner has linear and logarithmic amplifiers, 12-bit analog-to-digital converters, and 12-bit input and 8-bit output one-dimensional look-up tables. Its settings were adjusted via a plug-in module written by Howtek for Adobe Photoshop. The gamma values in this plug-in module were set to 1.8 to minimize quantization errors in the shadow regions of photographic prints. In addition, this resulted in reasonable tone reproduction when the images were viewed on a Macintosh computer system. The gamma setting rewrites the 12-bit to 8-bit one-dimensional look-up tables according to the selected setting. The reflective photographic samples were scanned at 307-dpi resolution that provides no interpolation data. Data were collected at 8-bit depth. No sharpness enhancement was adopted.

Input Target. As a reflective input material, a Fujix Pictography 3000 printer, a continuous tone three-dye printer, was used as the input medium. The decision for its use was its similarity to conventional photographic input and the ease with which one can produce samples. A target was prepared based on a $6 \times 6 \times 6$ factorial design in digital space plus an 18-step gray scale in 15 digital count increments. The digital image was output onto the reflective paper of the printer at 400 dpi resulting in a final $4" \times 5"$ print.

Metrology. The spectral reflectance factor of the input and output samples was measured using a Gretag SPM 60 spectrophotometer. This instrument has $45^\circ/0^\circ$ geometry, illumination simulating D_{65} , and a 10-nm sampling increment and bandpass. Each sample was measured in contact with a black mat surface. Colorimetric data were calculated from the spectral data using the ASTM tristimulus weights¹² for illuminant D_{65} and the 1931 2° standard observer.

Printer Forward Model

A model was desired that accurately predicted the spectral reflectance factor of colors formed using the proofing system from dot area ratios. In this proofing system, the probabilities of each dot are calculated by the Demichel equations.¹³

Test of First-Order Model. Expansion of *n*-Modified Neugebauer Equations with Dot-on-Dot Model Concept. Pobboravsky and Pearson proposed an adapted version¹⁴ of the Neugebauer equations¹⁵ to predict colors formed by pseudo-random halftone printers (e.g., rotated screens) in which the Murray-Davies equation modified by the Yule-Nielsen *n* value is applied to the original Neugebauer form to improve accuracy. This concept is shown in Eqs. 1 and 2.

$$\begin{aligned}
 R = & (a_c R_c^{1/n} + a_m R_m^{1/n} + a_y R_y^{1/n} + a_k R_k^{1/n} \\
 & + a_r R_r^{1/n} + a_g R_g^{1/n} + a_b R_b^{1/n} \\
 & + a_{ck} R_{ck}^{1/n} + a_{mk} R_{mk}^{1/n} + a_{yk} R_{yk}^{1/n} \\
 & + a_{rk} R_{rk}^{1/n} + a_{gk} R_{gk}^{1/n} + a_{bk} R_{bk}^{1/n} \\
 & + a_{cm} R_{cm}^{1/n} + a_{cm} R_{cm}^{1/n} + a_w R_w^{1/n})^n,
 \end{aligned} \tag{1}$$

$$\begin{aligned}
a_c &= c(1-m)(1-y)(1-k) \\
a_m &= (1-c)m(1-y)(1-k) \\
a_y &= (1-c)(1-m)y(1-k) \\
a_k &= (1-c)(1-m)(1-y)k \\
a_r &= (1-c)my(1-k) \\
a_g &= c(1-m)y(1-k) \\
a_b &= cm(1-y)(1-k) \\
a_{ck} &= c(1-m)(1-y)k \\
a_{mk} &= (1-c)m(1-y)k \\
a_{yk} &= (1-c)(1-m)yk \\
a_{rk} &= (1-c)myk \\
a_{gk} &= c(1-m)yk \\
a_{bk} &= cm(1-y)k \\
a_{cmy} &= cmy(1-k) \\
a_{cmk} &= cmyk \\
a_w &= (1-c)(1-m)(1-y)(1-k),
\end{aligned} \tag{2}$$

where a_i are the effective dot areas of the 16 Neugebauer primaries for four-color printing, described by the Demichiel equations;¹³ R_i are the reflectance factors of each i 'th Neugebauer primary, and c , m , y , and k are dot areas of each primary ink.

In Part I, we proposed a model that predicted the spectral reflectance factor of colors formed using an ink-jet printer employing a dot-on-dot halftone algorithm. This model was the spectral Murray-Davies-Yule-Nielsen model in which the n value was assumed to vary as a function of wavelength. This modification improved prediction accuracy appreciably compared with the usual n value shown in Eq. 1. The Part I model can be extended to four-color printing, shown in Eq. 3.

$$\begin{aligned}
R_\lambda &= (a_c R_{\lambda,c}^{1/n_\lambda} + a_m R_{\lambda,m}^{1/n_\lambda} + a_y R_{\lambda,y}^{1/n_\lambda} + a_k R_{\lambda,k}^{1/n_\lambda} \\
&+ a_r R_{\lambda,r}^{1/n_\lambda} + a_g R_{\lambda,g}^{1/n_\lambda} + a_b R_{\lambda,b}^{1/n_\lambda} \\
&+ a_{ck} R_{\lambda,ck}^{1/n_\lambda} + a_{mk} R_{\lambda,mk}^{1/n_\lambda} + a_{yk} R_{\lambda,yk}^{1/n_\lambda} \\
&+ a_{rk} R_{\lambda,rk}^{1/n_\lambda} + a_{gk} R_{\lambda,gk}^{1/n_\lambda} + a_{bk} R_{\lambda,bk}^{1/n_\lambda} \\
&+ a_{cmy} R_{\lambda,cmy}^{1/n_\lambda} + a_{cmk} R_{\lambda,cmk}^{1/n_\lambda} + a_{w\lambda,w}^{1/n_\lambda})^{n_\lambda}.
\end{aligned} \tag{3}$$

Using SYSTAT¹⁶, n_λ in Eq. 3 and the statistical effective dot areas (c , m , y , and k in Eq. 2) were optimized for cyan, magenta, yellow, and black ramps in which each ramp had 15 steps between white and the maximum ink amount. Previously,¹ the optimization was performed successively where c , m , y , and k were first defined by their theoretical values while optimizing n_λ . Once n_λ was estimated, the effective dot areas were optimized using the estimated values for n_λ . This restriction was not applied in this research. Figure 1 shows the optimized result of n_λ . Figure 2 shows the statistical effective dot areas of the magenta ramp as a representative example. The positive dot-gain (curvature) represents both optical and mechanical dot gain. It seems that the statistical effective dot areas model global dot-gain behavior while n_λ compensates for variances in dot area that are wavelength dependent. It seems reasonable that optical effects are wavelength dependent. The measured spectral reflectance factor data for the magenta ramp and their predictions using Eq. 3, the optimized n_λ , and their statistical effective dot areas are plotted in Fig. 3. Clearly the predicted curves fit the measured data well. The average color difference between the measured and predicted colors of the magenta ramp was $0.9 \Delta E_{ab}^*$ with a maximum of 2.7.

The relationship between statistical effective dot areas and theoretical dot areas of each primary ramp, $d_{ep,i}$, was

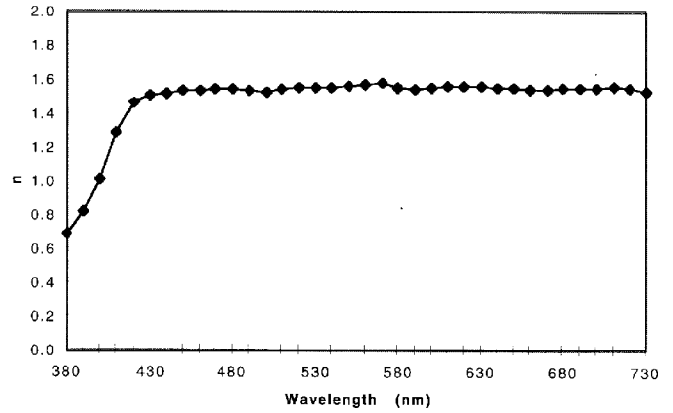


Figure 1. Optimized n_λ for ramps of four primary colors.

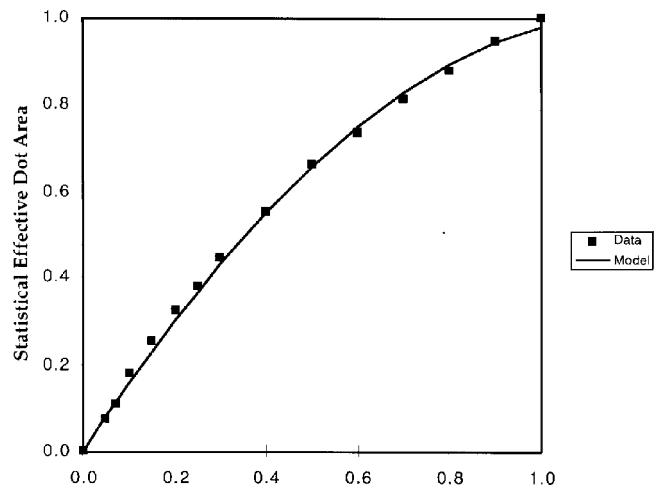


Figure 2. Relationship between theoretical dot area and statistically derived effective dot. Line joined data are derived by a secondary polynomial model.

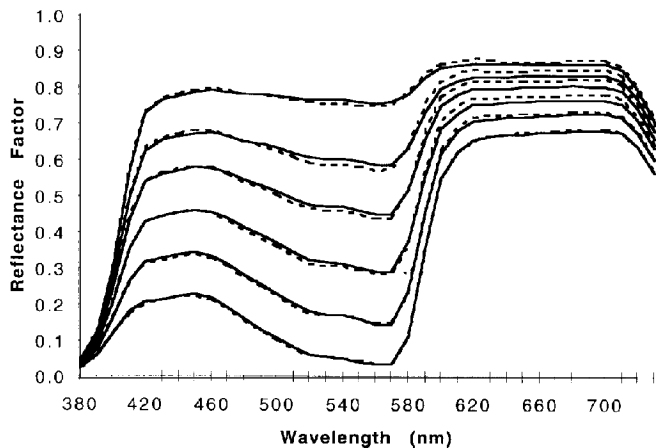


Figure 3. Measured spectral reflectance factor (dashed line) and predicted spectral reflectance factor (solid line) of the magenta ramp based on Eq. 1.

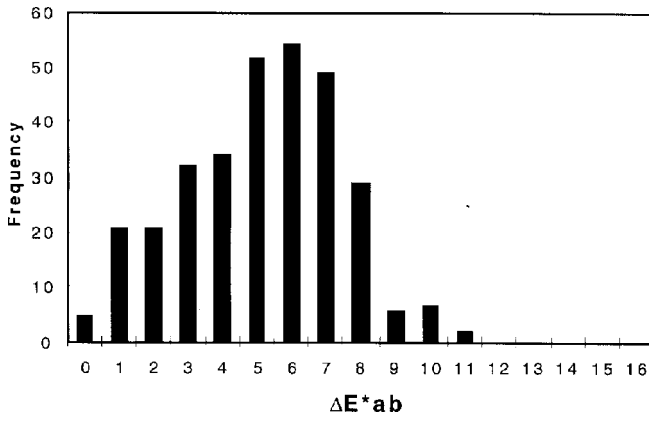


Figure 4. Color difference histogram of model performance based on the initial model.

modeled using second-order polynomial equations, described by Eq. 4. An example of the model fit is shown as a line in Fig. 2.

$$d_{ep,i} = \alpha_1 d_{t,i} + \alpha_2 d_{t,i}^2, \quad (4)$$

where $d_{t,i}$ is a theoretical dot area of primary color i , $d_{ep,i}$ is a statistical effective dot area optimized from a primary color ramp, and α_1 and α_2 are model coefficients. These modeled statistical effective dot areas, $d_{ep,i}$, were adopted as dot areas of primary colors in Eq. 2 (e.g., $c = d_{ep,c}$). The prediction performance of this equation for the four primary ramps was an average of $1.4 \Delta E_{ab}^*$ and a maximum of $4.6 \Delta E_{ab}^*$.

Performance of the First-Order Model. Using Eqs. 2 through 4 and n_i , the spectral reflectance factors of 325 colors sampling the color gamut of the proofing system were predicted. The average color difference was $5.6 \Delta E_{ab}^*$ with a maximum of $12.0 \Delta E_{ab}^*$. The color difference histogram and a projection vector diagram from measured to predicted colors on the CIELAB L^*-a^* plane are shown in Figs. 4 and 5, respectively. Figure 6 shows measured and predicted spectral reflectance curves, each having a large prediction error in CIELAB.

According to Fig. 4, the performance of the model in predicting the entire color gamut was poor in spite of providing extremely good prediction results for the four primary color ramps. The predicted colors, except those associated with the ramps, were almost always darker, which is seen in the vector directions shown in Fig. 5. Moreover, it is obvious from Fig. 6 that the predicted spectral reflectance factors were lower than the measured values. This error was caused by an overestimation of the effective dot areas except those of the four primary-color ramps. If the effective dot areas of secondary, tertiary, and quaternary colors were statistically estimated, it would show that the effective dot areas of each constituent primary have reduced area in comparison to their areas when printed individually. This behavior is similar to the phenomenon of ink trapping. Because ink trapping, ink spread, and dot-gain variation are negligible for this proofing system, this is optical effect, to be referred to as “optical trapping,” caused by the overlapping of other ink layers. Clearly, the model must be modified to account for this phenomenological effect to achieve acceptable accuracy.

Modification of First-Order Model. Model of Optical Trapping. The difference between the effective dot area, d_e , and the theoretical dot area, d_t , is usually referred

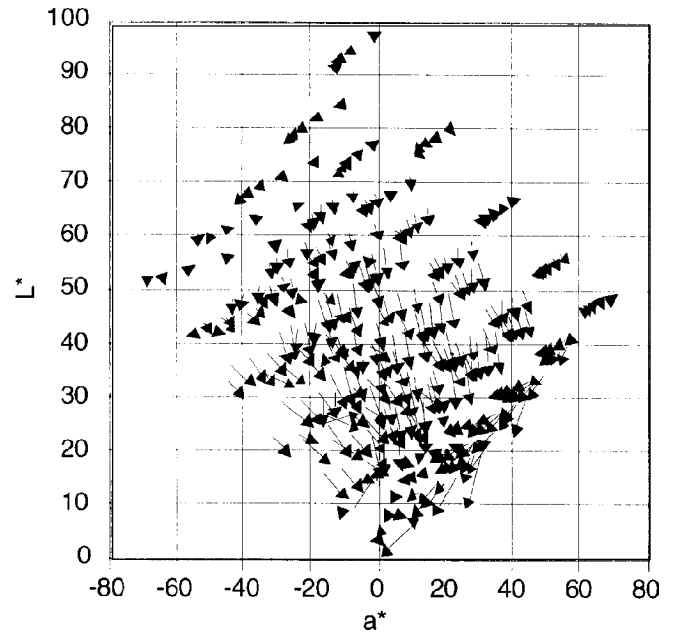


Figure 5. Error vector of predicted colors based on the initial model in L^*-a^* plane. Vector tail locates the measured coordinate; vector head locates the predicted coordinate.

to as dot gain, g , and expressed by Eq. 5. If dot gain is known, the effective dot area can be calculated using the inversion of Eq. 5, shown in Eq. 6.

$$g = d_e - d_t, \quad (5)$$

$$d_e = d_t + g. \quad (6)$$

Thus, the effective dot area can be described as a linear combination of two functions. This is useful when considering the optical trapping phenomenon. It was hypothesized that each ink had an inherent dot gain function characterized by evaluating primary ramp data. With overlapping inks, the extent of the dot gain varied, but not its fundamental shape. This hypothesis is illustrated in Fig. 7. The highest isocontour curve represents the dot gain of a primary color ramp. The lower curves show the reduction in dot gain caused by other ink layers. The particular curve depends on the ink and the amount of overlap.

Equation 7 describes the dot-gain functions depicted in Fig. 7.

$$g = qg_p = q(d_{e,p} - d_t) \quad 0 \leq q \leq 1, \quad (7)$$

where g_p describes the dot gain of a primary and $d_{e,p}$ is the statistical effective dot area of the primary. Coefficient q depends on the dot areas of other overlapping ink layers. Therefore, the statistical effective dot area, d_e , is calculated by Eq. 8.

$$d_e = d_t + qg_p. \quad (8)$$

The interaction between inks is illustrated in Fig. 8. The y axis defines the theoretical dot areas of an arbitrary primary (the overlapped ink); the z axis defines the dot gain of this primary; the x axis defines the theoretical dot area of another primary (the overlapping ink). Rotating Fig. 8 such that the observational point of view faces the y axis results in Fig. 7. Changes in the amount of the second primary (the overlapping ink) affect the extent of dot-gain,

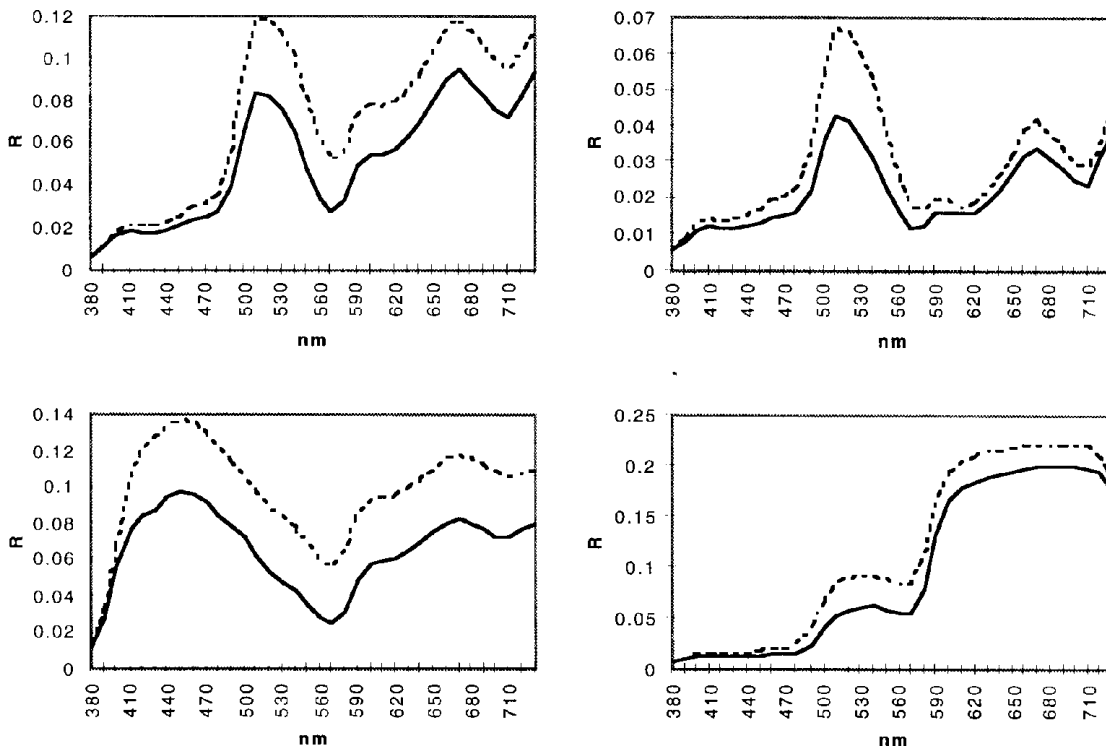


Figure 6. Measured reflectance factor (dashed line) and predicted factor (solid line), that has a large prediction error.

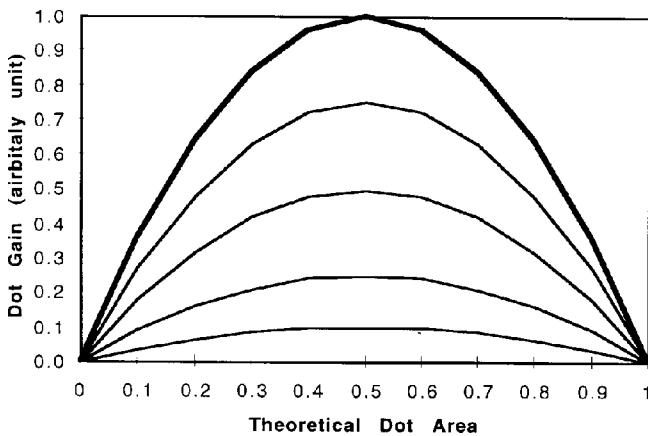


Figure 7. Schematic diagram of variation of dot-gain caused by overlapping other ink layers. In this study, it was assumed that dot-gain curves (thin line) had a similar shape as the primary non-overlapped one (thick line).

constrained by the fundamental dot-gain function of the arbitrary primary. The change in the extent of dot-gain is monotonically related to the amount of overlap of the second ink. Because the dot-gain of the arbitrary ink is greatest at 50% theoretical dot area, a function can be fit relating the theoretical area of the overlapping ink with the effective dot area of the primary (the overlapped ink). This is function q . Thus, for two inks, one needs samples that enable characterizing of g_p and q . Function g_p is characterized through analyzing the primary ramp data. Function q is characterized by overprint samples where the arbitrary primary is fixed at 50% theoretical dot area and the overlapping ink is varied.

In four-color printing, tertiary and quaternary overlapping can occur in addition to the secondary overlapping described above. We further hypothesized that the statistical

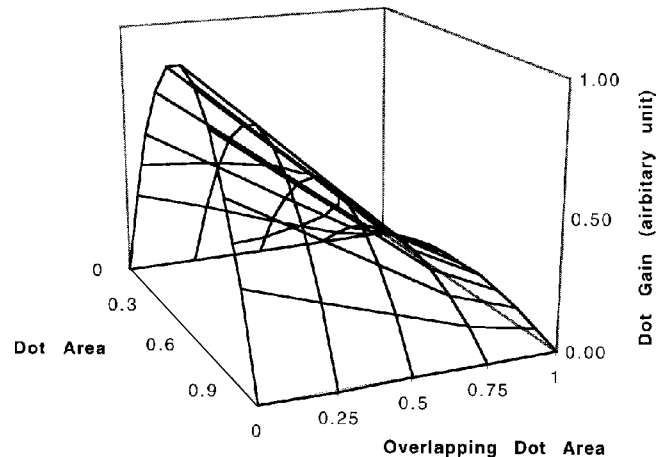


Figure 8. Model of decreasing dot-gain for secondary color. The z axis shows dot-gain of overlapped ink; the x axis shows theoretical dot area of overlapping ink; the y axis shows theoretical dot area of overlapped ink.

effective dot gain of more than secondary colors was expressed by the multiplication of each secondary color. When analyzing the first-order model, colorimetric errors increased with an increase in the number of overlapping inks. This is evident in Fig. 5. The error vectors increase in length in gamut regions corresponding to two-, three-, and four-ink colors. This observation led to this hypothesis. For example, coefficient q for cyan ink, q_c , is a product of the effects due to magenta, yellow, and black inks. The four-color ink-trapping hypothesis is expressed by Eq. 9.

$$\begin{aligned}
 q_c &= f_{c,m}(d_{t,m}) f_{c,y}(d_{t,y}) f_{c,k}(d_{t,k}) \\
 q_m &= f_{m,c}(d_{t,c}) f_{m,y}(d_{t,y}) f_{m,k}(d_{t,k}) \\
 q_y &= f_{y,c}(d_{t,c}) f_{y,m}(d_{t,m}) f_{y,k}(d_{t,k}) \\
 q_k &= f_{k,c}(d_{t,c}) f_{k,m}(d_{t,m}) f_{k,y}(d_{t,y}), \quad (9)
 \end{aligned}$$

TABLE I. Samples of Effective Dot Areas and Coefficient q Varied by the Overlapping Ink(s) in Secondary Colors with the Overlapped Ink Cyan and Overlapping Inks Magenta, Yellow, and Black.

Overlapped ink: cyan, overlapping ink: magenta

Theoretical Cyan	Dot area Magenta	Effective Cyan	Dot area Magenta	Coefficient q
0.500	0.000	0.629	0.000	1.000
0.500	0.250	0.613	0.320	0.876
0.500	0.500	0.597	0.605	0.752
0.500	0.750	0.592	0.809	0.713
0.500	1.000	0.594	1.000	0.729

Overlapped ink: cyan, overlapping ink: yellow

Theoretical Cyan	Dot area Magenta	Effective Cyan	Dot area Magenta	Coefficient q
0.500	0.000	0.629	0.000	1.000
0.500	0.250	0.636	0.325	1.054
0.500	0.500	0.637	0.615	1.062
0.500	0.750	0.641	0.815	1.093
0.500	1.000	0.642	1.000	1.101

Overlapped ink: cyan, overlapping ink: black

Theoretical Cyan	Dot area Magenta	Effective Cyan	Dot area Magenta	Coefficient q
0.500	0.000	0.629	0.000	1.000
0.500	0.250	0.592	0.316	0.713
0.500	0.500	0.537	0.606	0.287
0.500	0.750	0.503	0.812	0.023
0.500	1.000	0.500	1.000	0.000

where q_i is coefficient q for the overlapped ink i , the function $f_{i,j}(d_{i,j})$ is the decreasing effective dot-gain function of the secondary color (overlapped ink i by overlapping ink j), and $d_{i,j}$ is the theoretical dot area of each overlapping primary color.

Determining Model Parameters. The dot-gain at 50% theoretical dot area was selected as the point that represented typical dot gain variances because it is the most sensitive point of the dot-gain function. The dot-gain of primary colors was defined as the difference between the effective dot area that can be calculated from Eq. 4 and the theoretical dot area.

To obtain the variations of q , samples were prepared where the primary (the overlapped ink) was fixed at 50% theoretical dot area while a secondary (the overlapping ink) was varied in 25% theoretical dot area increments between 25% and 100%. This sampling design was repeated for each primary. An example of these dot-area combinations is shown in Table I, in which cyan is the primary (overlapped ink) and magenta, yellow, and black are the secondaries (overlapping inks).

Using the modified Neugebauer equation (Eq. 3) and SYSTAT, statistical effective dot areas were optimized for each sample. An example of the results of these optimizations is shown in Fig. 9 where cyan is the primary and magenta is the secondary. The complete data set for cyan is listed in Table I. It is obvious that the more the overlapping dot area increases, the greater the reduction in dot-gain. In addition, each secondary has a unique influence on a given primary. This was expected because each ink has unique optical properties.

The relationships exemplified in Fig. 9 led to the use of second-order polynomials with a fixed intercept at unity

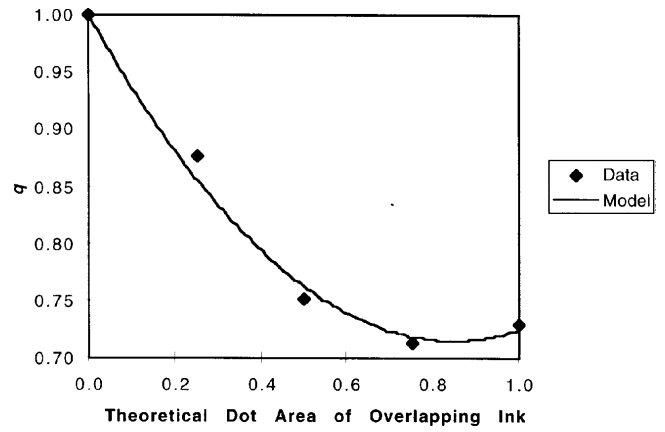


Figure 9. An example of q variations varied by overlapping ink in a secondary color, $f_{c,m}(m)$: Overlapped ink is cyan; overlapping ink is magenta. Also a second-order polynomial model describing these q values.

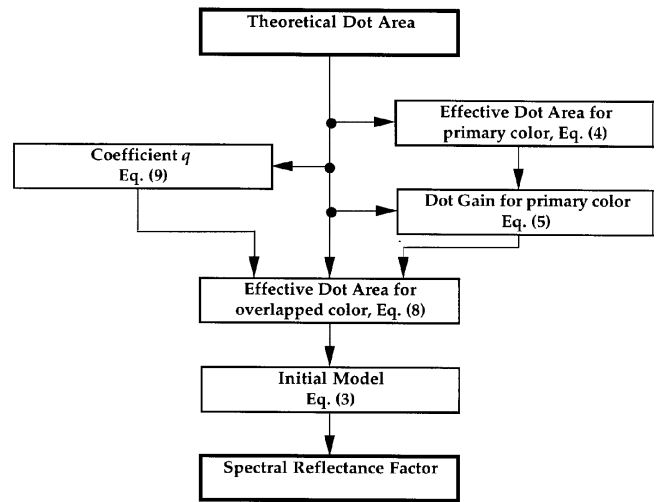


Figure 10. Data flow of modified Neugebauer equations with a correction for optical trapping.

to model each q value change. This function is shown as Eq. 10 where $\beta_{i,j}$ are model coefficients. The solid line shown in Fig. 9 typifies the model fit using Eq. 10.

$$f_{i,j}(d_{i,j}) = 1.0 + \beta_{i,j,1}d_{i,j} + \beta_{i,j,2}d_{i,j}^2. \quad (10)$$

Performance of the Modified Model. A flow chart of the complete forward model is shown in Fig. 10. Using this model, the spectral reflectance factors of the verification target were predicted. The average color difference of the 325 samples was $2.2 \Delta E_{ab}^*$ with a maximum of $5.5 \Delta E_{ab}^*$. The color difference histogram and vector plots for each CIELAB plane are shown in Figs. 11 and 12, respectively. The samples exhibiting large spectral error based on the initial model (Fig. 6) are replotted in Fig. 13 using the modified model. Statistical comparisons between the first-order and modified models are listed in Table II. The addition of the optical trapping model resulted in obvious improvement.

The model of “ink trapping” developed in this research is based on a phenomenological approach where we modeled the obvious systematic errors in the reconstructed spectral data for ink mixtures based on a reasonable first-order model. Clearly, this interaction model must have

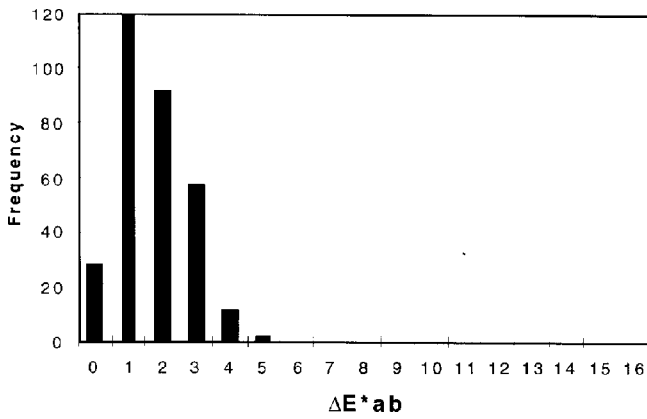


Figure 11. Color difference histogram of model performance based on the initial model with a correction for optical trapping.

some relationship to the actual optics of this proofing system. Research described in Refs. 17 through 21 point to pathways that link the observed phenomena with the absorption and scattering properties of printing. Given the high colorimetric accuracy of the model developed in this research, it might be used as a simulation tool for more basic research.

Printer Backward Model

One objective of this research was to develop a black printer model with similar characteristics to conventional color-separation methods. The first step was to evaluate the tone reproduction characteristics of each primary resulting from conventional color separation. These tend to be generated empirically and are referred to as gradation curves in the printing industry.²² The second step was to integrate these characteristics into a colorimetric color reproduction paradigm. Finally, the forward model described in the previous section along with the black printer model was inverted using an iteration method to build a device profile for this proofing system.

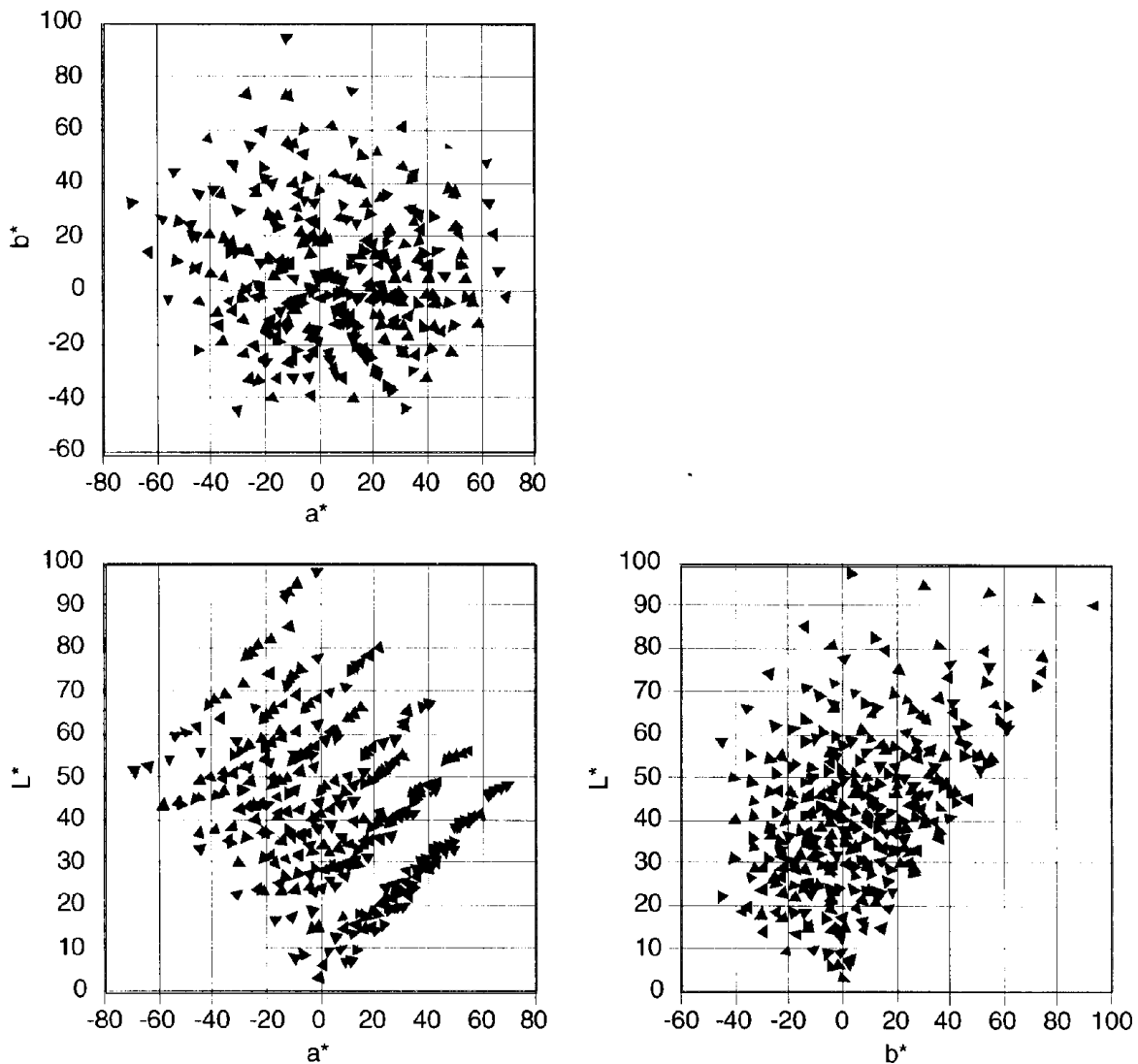


Figure 12. Error vector of predicted colors based on the initial model with a correction for optical trapping. Vector tail locates the measured coordinate; vector head locates the predicted coordinate.

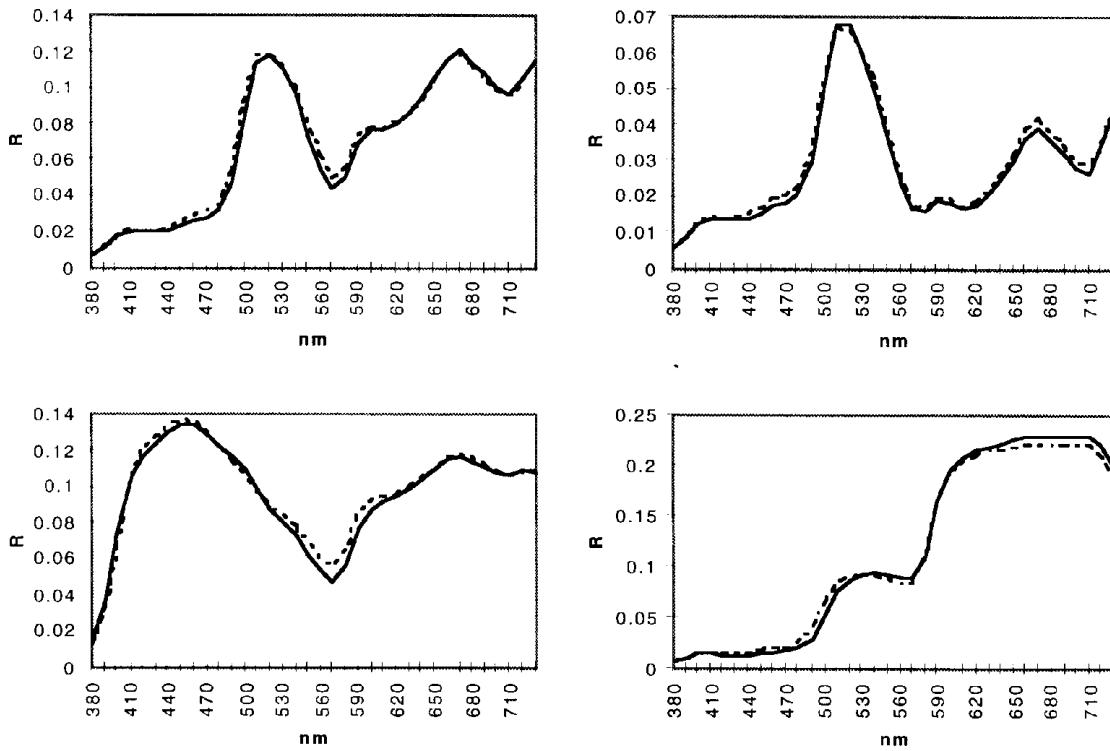


Figure 13. Measured reflectance factor (dashed line) and predicted reflectance factor (solid line) of samples that have a large prediction error in the initial model.

TABLE II. Color Difference Statistics for Predicted Colors Using the Initial Model and the Modified One

Statistics	Initial model	Modified model
Average ΔE^*_{ab}	5.6	2.2
Maximum ΔE^*_{ab}	12.0	5.5
Standard deviation ΔE^*_{ab}	2.3	1.0

Black Printer Model. The following equation often is suggested⁴ for the separation model of the black printer that includes²² a UCR concept.

$$\begin{aligned}
 k' &= b \cdot \min(c, m, y) \\
 c' &= c - u \cdot k' \\
 m' &= m - u \cdot k' \\
 y' &= y - u \cdot k' \\
 0 &\leq b \leq 1 \\
 0 &\leq u \leq 1,
 \end{aligned} \tag{11}$$

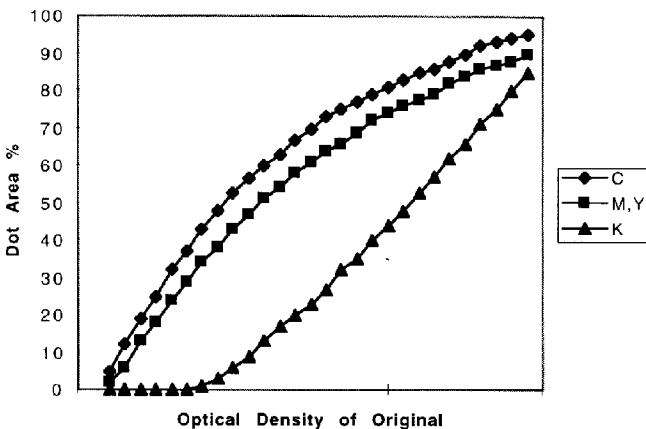


Figure 14. An example of tone reproduction curves used in conventional color-separation methods.

where b represents a black rate, u represents an under-color-removal rate, and the prime superscript represents the four-color separations following UCR. These equations are performed in the dot area or in a device-drive signal-space directory. However, these are qualitative expressions and are not generally good for practical use because the replaced dot area or drive signal of the black print does not have a linear relationship with the corresponding replacement of cyan, magenta, and yellow. In addition, an equivalent dot area or an equivalent drive signal of cyan, magenta, and yellow do not maintain gray balance. These limitations lead to the use of optical-density-based tone reproduction or gradation curves,^{13,23} as shown in Fig. 14. These are based on the concepts described by Eq. 11, but adjusted to maintain gray balance.

It is assumed that these functions, based on the ideal optical density, s , of gray steps to the dot area, are expressed by $h(s)$. A gray step that has density s is reproduced by a combination of $h_c(s)$, $h_m(s)$, $h_y(s)$, and $h_k(s)$ dot-areas. If the dot area of black ink is determined as k , the original density relating to the black ink can be calculated using the inverse function, $h_k^{-1}(k)$. Applying a UCR concept, at least one of the densities relating to the three

chromatic inks should be the same as that of the black ink. Original densities relating to the other two inks should be more than that of the black ink. These relationships are expressed in Eq. 12.

$$\begin{aligned}
 s_k &= h_k^{-1}(k) \\
 s_c &\geq s_k, s_m \geq s_k, s_y \geq s_k \\
 s_k &= \min(s_c, s_m, s_y) \\
 c &= h_c(s_c) \\
 m &= h_m(s_m) \\
 y &= h_y(s_y)
 \end{aligned} \tag{12}$$

Inversely, if the dot areas of cyan, magenta, and yellow are determined, the original densities relating to these three inks are calculated using the inverse functions. Using the UCR concept in density space, it is possible to conclude that the original density of black ink, s_k , corresponds to the minimum of the other three densities. Therefore, the dot area of black ink can be calculated using this minimum density and the forward function $h_k(s_k)$. These transformations are shown in Eq. 13.

$$\begin{aligned}
 s_c &= h_c^{-1}(c) \\
 s_m &= h_m^{-1}(m) \\
 s_y &= h_y^{-1}(y) \\
 s_k &= \min(s_c, s_m, s_y) \\
 k &= h_k(s_k),
 \end{aligned} \tag{13}$$

where s_i is the original density of the tone reproduction curves corresponding to ink i . In this research, third-order polynomial equations were used to define the relationships between dot area and density, according to Fig. 14.

The dot area of black ink is defined automatically using Eq. 13 once the dot areas of cyan, magenta, and yellow are determined. In other words, the dot area of black ink is not arbitrary, but is subordinated to the dot areas of the other three inks through the medium of tone reproduction curves. Moreover, because the calculation of dot areas in this method is not performed in the dot-area space directly, it is expected that a colorimetric match is provided and that this black printer model has similar characteristics to conventional color-separation methods used with prepress scanners.

Implementation of Backward Model. A direct search method, the Simplex method, was selected as an iterative technique to invert the printer forward model numerically. As described in Part I, the Simplex method was more stable and robust than derivative-based methods such as the Newton-Raphson method for use with analytical-based printer models.

Starting values were defined based on a pixel's aim tristimulus values, X , Y , and Z ; this is shown in Eq. 14,

$$\begin{aligned}
 c &= 1 - X/X_n \\
 m &= 1 - Y/Y_n \\
 y &= 1 - Z/Z_n,
 \end{aligned} \tag{14}$$

where X_n , Y_n , and Z_n are tristimulus values of the reference illuminant. The initial simplex was defined according to Eq. 15.

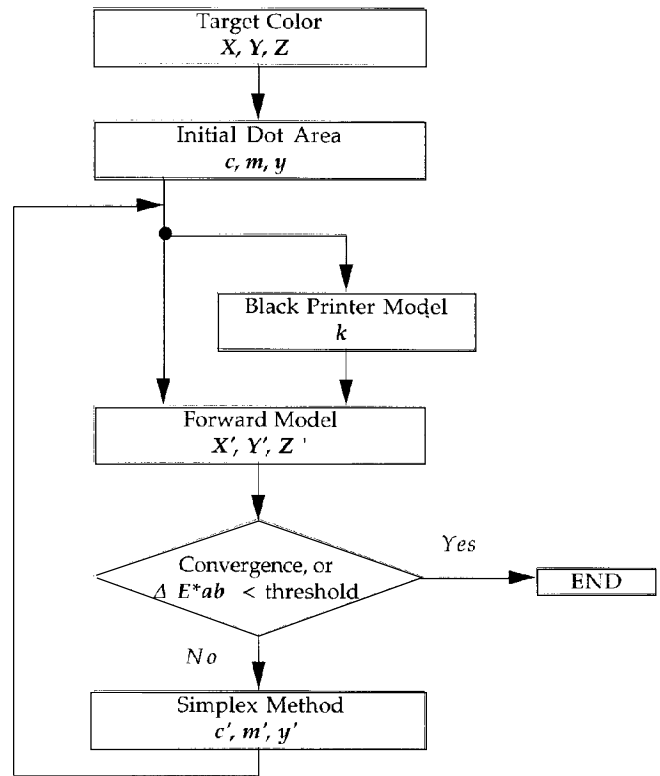


Figure 15. Data flow of the backward model that includes the forward model, the black printer model, and the Simplex method.

$$\begin{aligned}
 P_0 &= [c, m, y] \\
 P_1 &= [c, s_1, m + ls_2, y + ls_3] \\
 P_2 &= [c + ls_1, m + s_2, y + ls_3] \\
 P_3 &= [c + ls_1, m + ls_2, y + s_3],
 \end{aligned} \tag{15}$$

where

$$\begin{aligned}
 l &= 1 / (\sqrt{n+1} + 2), n = 3, \\
 s_i &: \text{scale factors.}
 \end{aligned}$$

The dot area of black ink was defined by the above dot areas using Eq. 13. The range of dot areas was limited between 0 and 1.0 using a sawtooth function¹ before progressing through the forward model to obtain an existing approximated root. The calculation was terminated if the difference between the best and the worst simplex of each ink was less than 0.001 (less than half of the quantization unit when the range of dot area is divided to 8 bit). The other conditions were the same as described in Part I. The data flow of this backward model is shown in Fig. 15.

Performance of the Backward Model. Influence of the Dot Area Transformation Function. The similarity to conventional methods, calculation stability, and convergence problems of this backward model were certified under various conditions.

Changing the dot area of each ink was investigated in the CIELAB space. Using the backward model, dot areas were calculated in which two CIELAB coordinates were fixed and the other varied systematically. The results of these calculations are shown in Fig. 16. In Fig. 16(a), a^*

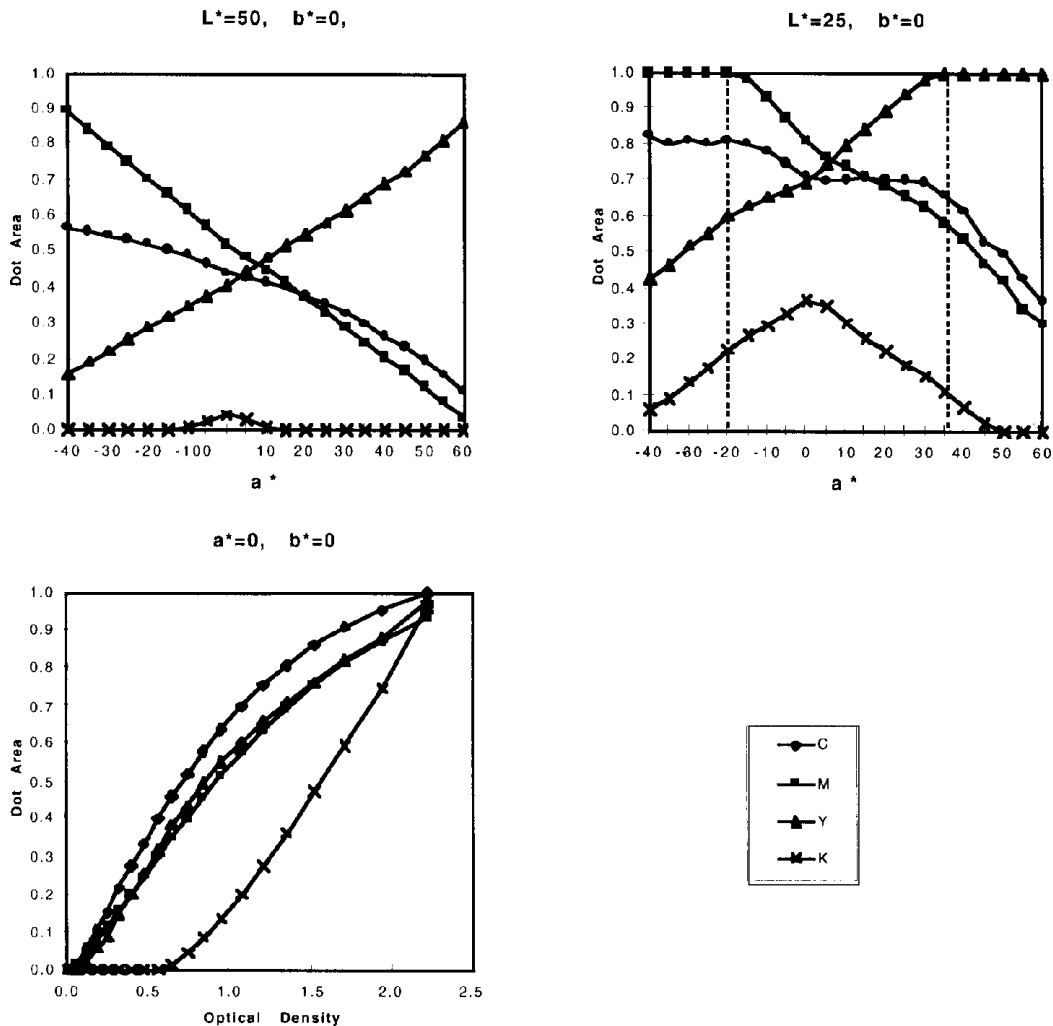


Figure 16. Dot area of each ink to reproduce color gradations, (a) a^* change at $L^* = 50$ and $b^* = 0$, (b) a^* change at $L^* = 25$ and $b^* = 0$, (c) L^* change at $a^* = 0$ and $b^* = 0$. Dashed lines indicate boundaries between reproducible and nonreproducible colors in this model.

was varied while b^* equaled 0 and L^* equaled 50. In Fig. 16(b), a^* was varied while b^* equaled 0 and L^* equaled 25. The curves are reasonably smooth indicating that the Simplex method did not oscillate or diverge from the optimal solution. Note that some of the target CIELAB coordinates were outside of the proofing system's color gamut. These results were consistent with the evaluations performed in Part I. Furthermore, the color separations exhibited similar characteristics to traditional UCR; as the CIELAB coordinates progressed toward neutral, the amount of black ink increased. Fig. 16(c) is a plot of dot area versus optical density in which L^* was changed from 5 to 100 while a^* and b^* were fixed at 0. In comparison with Fig. 14, Fig. 16(c) has obvious similar transformation characteristics to conventional tone reproduction curves.

Similarity to Conventional Methods. It is expected that this backward model results in characteristics similar to conventional methods as indicated by Fig. 16(c). However, only achromatic colors were evaluated. To confirm the similarity for the entire color gamut, the following comparison was performed. The Kodak Q-60R1 scanning target was color separated into four-color dot areas using a conventional prepress scanner. In this experiment, the Crosfield Magnascan 656 was used. These digital data were transformed to tristimulus values using the forward model. The tristimulus values were again

transformed to four-color dot areas using the backward model. Finally, the four-color dot areas obtained by the conventional method and the backward model were compared. The flowchart of this process is shown in Fig. 17.

The dot areas of each color patch of the scanned Q-60R1 digital image were averaged and converted to dot areas of the backward model as shown in Fig. 17. Correlations of each ink are shown in Fig. 18. Obviously the cyan and magenta dot areas obtained by the backward model are highly correlated with those obtained by the conventional method. However, the dot areas of yellow and black inks deviated slightly. Calculations of this black printer model were performed in a colorimetric space. Therefore, deviations of the dot areas of yellow ink might be large and the dot areas of black ink were affected by those deviations. In addition, the specific separation algorithm used with this Crosfield system might be more complicated than the simple method used in this research. Correlation coefficients of cyan, magenta, yellow and black inks were 0.999, 0.999, 0.995, and 0.960, respectively. The combined *CMYK*, combined *CMY*, and isolated *K* images of the Q-60R1 obtained by both methods are shown in Fig. 19. In this *CMYK* to *CMYK* image conversion, a color management module (in which dot areas obtained by a conventional prepress scanner were the input and those obtained by the backward model were the output) was built in advance as a 8 bit-depth four-dimensional look-up table for $11 \times 11 \times 11 \times 11$ factorial

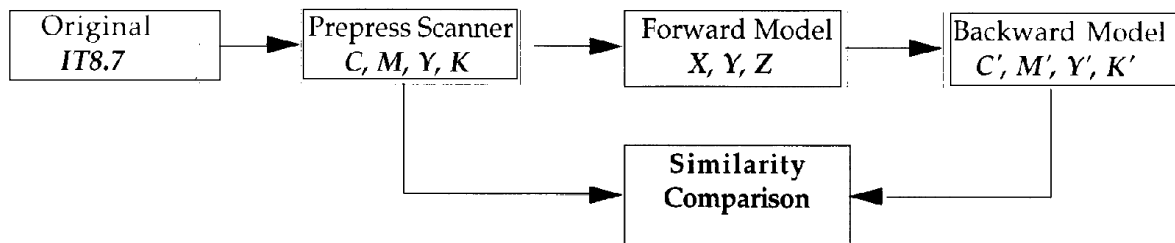


Figure 17. Flowchart of data to certify the similarity of this backward model to a conventional color-separation method.

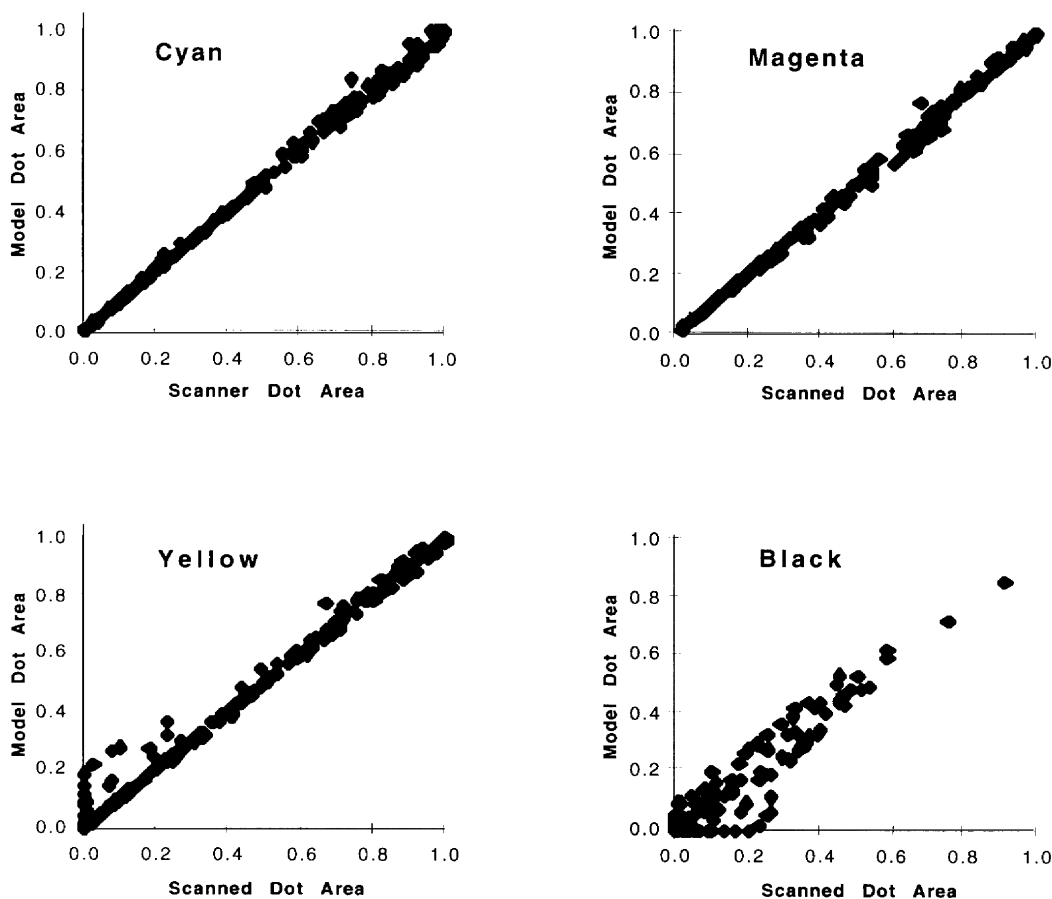


Figure 18. Correlation between dot area obtained by a conventional color-separation method and dot area obtained by the backward model.

dot area design input sampling. According to the images of the black ink in Fig. 19, the backward model shows very similar characteristics except in very dark color regions. These differences might be owing to differences in the tone reproduction curves between the two methods. The standard tone reproduction curves are changed for each input image during scanner set-up. Also, the Fig. 14 curves were obtained when the UCR switch of the prepress scanner was turned off (because tone reproduction curves of prepress scanners are commonly adjusted when the UCR switch is turned off). However, the Fig. 19 image was scanned with the UCR switch turned on, also a common practice. If the UCR settings were matched, greater similarity in tone reproduction would be expected.

Scanner Forward Model

A similar approach to that of Berns and Shyu²⁴ was used to estimate tristimulus values of a given set of scan-

ner digital counts. In both methods, the spectral reflectance factors of the reflective material were reconstructed from scanned data using the Kubelka–Munk color mixture model for opaque materials. The difference from Berns and Shyu was the evaluation method of dye concentrations from digital data. They directly related the logarithm of the normalized digital counts to analytical dye concentrations using high-order polynomial functions. However, the digital data obtained by scanning the input target must be related to the reflectance factor of the input target that corresponds to integrated dye concentrations (absorbance), rather than analytical dye concentrations. Therefore, scanned digital data were first transformed to reflectance data, and then transformed to theoretical integrated concentration data using the Kubelka–Munk theory. This transformation assumed that the spectral responsivities of each channel of the scanner were 20 nm with a rectangular bandpass centered at



(a)

(b)

Figure 19. IT8.7/2 target images obtained by (a) conventional method and (b) by the backward model including the black printer model. These images were printed out with the Pictography 3000. Data of dot areas (CMYK) were transformed to RGB signals and these were exported to the Pictography 3000 using Adobe Photoshop.

the peak absorptivities of each dye. Even though this assumption deviates significantly from the actual scanner's spectral responsivities, it is possible to compensate for this difference at the transformation step from integrated concentrations to analytical concentrations using higher order polynomial functions rather than a linear transformation. Essentially, the method used in the current research followed a more theoretical pathway than that used previously. Details of this improved method are described in Appendix A.

Tristimulus values were calculated from both measured and predicted spectral reflectance factor data for illuminant D_{65} and the CIE 2° observer for all of the color patches of the Fuji Pictography color target. Using a 3×3 matrix for conversion from theoretical integral concentrations to analytical concentrations resulted in an average ΔE^*_{ab} of 0.9 with a maximum of 3.0. Using a 3×11 matrix resulted in an average ΔE^*_{ab} of 0.8 with a maximum of 2.4. Both color difference histograms are shown in Figs. 20(a) and 20(b), respectively. The difference in

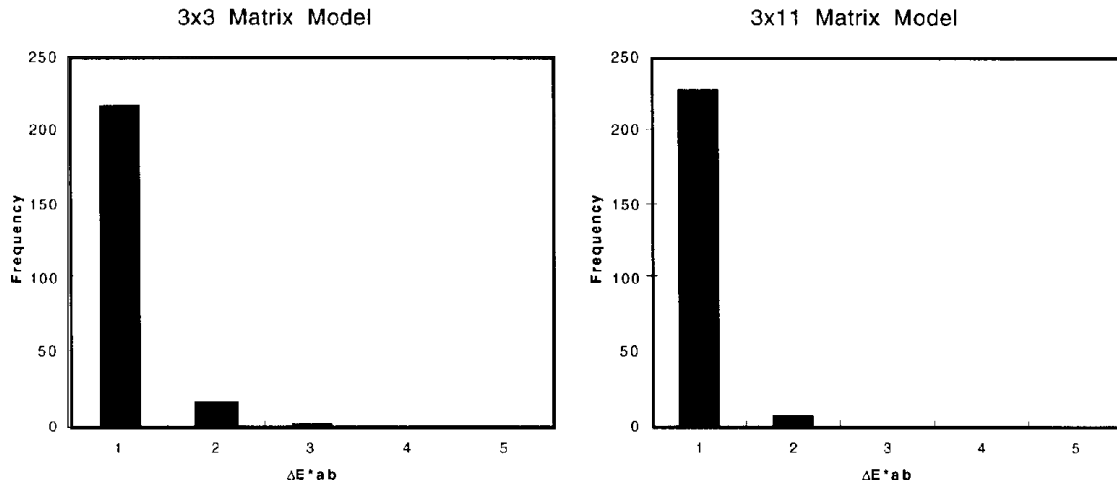


Figure 20. Color difference histogram of scanner forward model performance; (a) based on 3×3 matrix and (b) based on 3×11 matrix.

performance was not significant. The 3×3 matrix was selected as the transformation from theoretical integral concentrations to analytical concentrations in this research because of its higher accuracy for achromatic colors.

Building the Device Profile and Its Evaluation

To evaluate the backward model for practical use, a concatenated color management module (in which the scanner digital counts d_r, d_g, d_b were the input and those related to dot area of Matchprint d_c, d_m, d_y, d_k were the output) was built as a 8-bit-depth multidimensional color look-up table for a $33 \times 33 \times 33$ factorial digital design input sampling. No white point matching was adopted between the original and reproduction substrates. Also, minimum ΔE^*_{ab} clipping was adopted as a gamut mapping technique in the concatenated CMM. This gamut mapping strategy is useful when evaluating the colorimetric accuracy of CMMs because common gamut colors are left unchanged. Furthermore, the mapping technique validates the computational robustness of the Simplex algorithm for out-of-gamut colors.

A reproduced IT8.7/2 target using the Pictography 3000 (generated by scanning an actual IT8.7/2 target and simply printing the digital file with default color management) was used as an independent original to evaluate the system performance. This reproduced IT8.7/2 target was scanned by the D4000 at 307-dpi resolution. Using the CMM module described above and the RITRC 3DLUT plug-in software²⁵ for Adobe Photoshop, the image data were transformed to the dot area data for Matchprint.

The projected colorimetric error vectors between the target and its reproduction are shown in Fig. 21. The average ΔE^*_{ab} was 2.1 with a maximum ΔE^*_{ab} of 9.7. The maximum color difference was larger than that of the forward model because the color management module included errors owing to the scanner model as well as effects due to differences in color gamut between the Pictography and Matchprint. Comparing Figs. 12 and 21, a clear difference exists in color gamut between these two devices. Excluding these out-of-gamut colors reduced the average ΔE^*_{ab} to 1.3 with a maximum ΔE^*_{ab} of 4.5. Color difference histograms both including and excluding out-of-gamut colors are shown in Figs. 22(a) and 22(b). Color difference statistics of the CMM are listed in Table III.

TABLE III. Color Difference Statistics Categorized by Printer Gamut

	Pictography input target colors	
	All colors	Colors inside gamut
Average ΔE^*_{ab}	5.6	2.2
Maximum ΔE^*_{ab}	12.0	5.5
Standard deviation ΔE^*_{ab}	2.3	1.0

Conclusions

A spectral-based model, which was derived for a dot-on-dot printer,¹ was expanded to include halftone random-dot printers. This model was a modified spectral Neugebauer model in which n was assumed to vary as a function of wavelength. Model parameters, n_λ and effective dot areas were optimized statistically for ramps of each primary color. It seemed that the differences between statistical effective dot areas and their theoretical values related to global dot-gain behavior while variations in n_λ compensated for global wavelength-dependent optical behavior. Predictions for these primary ramps fit measured spectral reflectance factor data well. However, colors sampling the entire color gamut were poorly predicted because of an overestimation of each primary's effective dot area. The effective dot area of a given primary decreased as a function of the amount of overlap of other primaries. This behavior is similar to the printing phenomenon of ink trapping. Because ink trapping could not occur in the proofing system used in this research, the effect is optical in origin and was referred to as "optical trapping" in this research. A phenomenological model was derived that predicted this optical interaction. The addition of this model of optical trapping improved the prediction accuracy significantly, resulting in an average ΔE^*_{ab} of 2.2 with a maximum ΔE^*_{ab} of 5.5.

A black printer model was derived with similar behavior to conventional color separations based on the concept of UCR while providing colorimetric matching. The forward spectral-based model and the black printer model were inverted to build a device profile. The direct search method, the Simplex algorithm, was used for the numerical inversion. The robustness of the Simplex method and the similarity of the black printer model to convention color separation were verified for several conditions of usage.

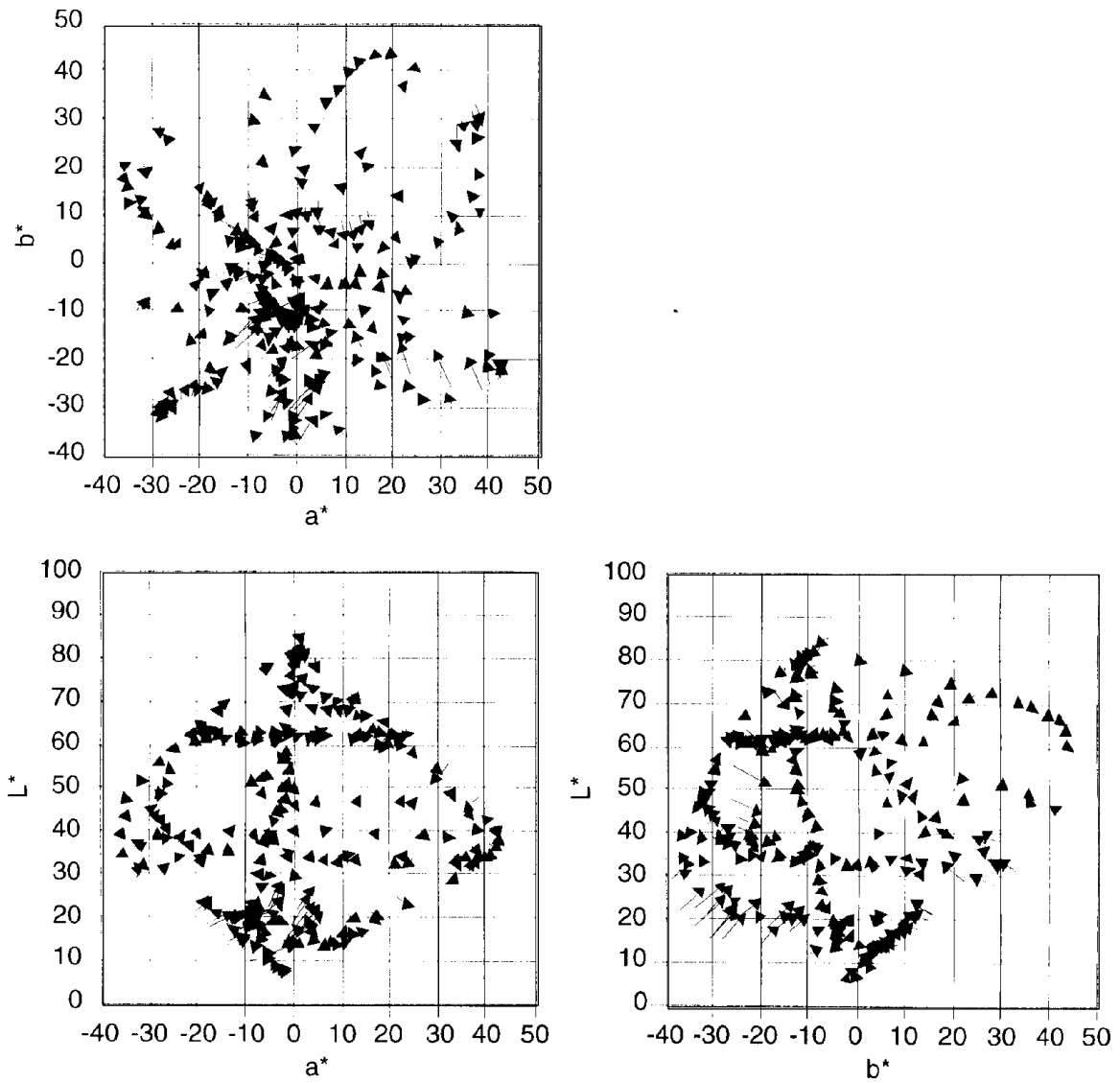


Figure 21. Error vector of reproduced colors by a concatenating color management module. Vector tail locates target coordinate; vector head locates reproduced coordinate.

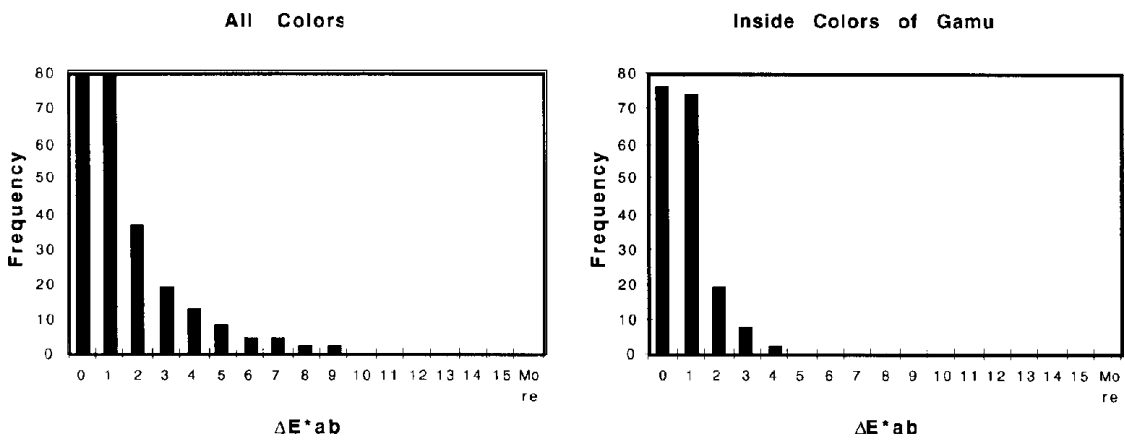


Figure 22. Color difference histogram of reproduced colors using a concatenating color management module: (a) includes colors outside of the gamut and (b) excludes colors outside of the gamut.

It was not verified whether the black printer model derived in this research maximizes the color gamut of this proofing system. This would be a useful future analysis.

A spectral reconstruction method, based on research by Berns and Shyu, was used to convert digital to colorimetric data for Fujix Pictography 3000 reflection images scanned on a Howtek D4000 drum scanner. The method used in this research adopted two stages to convert from digital data to theoretical integrated dye concentrations where the scanner was assumed to have narrow rectangular bandpass spectral responsivities. This resulted in improved performance and a device profile with an average ΔE^*_{ab} of 0.9 with a maximum of 3.0.

A CMM was made by concatenating the scanner device profile, a minimum ΔE^*_{ab} gamut mapping technique, and the printer inverse model. The CMM was an 8-bit-depth multidimensional 33³ CLUT in which digital counts of the scanner were the input and those related to dot area of the color proofing system were the output. The performance was evaluated by comparing an independent Pictography image of an IT8.7/2 target with its reproduction proof. For the entire target, the average ΔE^*_{ab} was 2.1 with a maximum of 9.7. Excluding out-of-gamut colors, the performance reduced to an average ΔE^*_{ab} was 1.3 with a maximum of 4.5.

Several conclusions can be drawn from this research. Device profiles can be easily built for a color proofing system for offset printing by printing and measuring a test target of 42 secondary colors, the 16 Neugebauer primary colors, and ramps of each four primary colors. Similar black printer characteristics to that of conventional color-separation systems can be obtained within a colorimetric framework. Furthermore, this black printer model has the advantage of not requiring regional search techniques sometimes necessary.^{4,5} However, this reduction in complexity may be at the expense of a slightly reduced color gamut. This is an area for further investigation. Finally, future research should investigate the relationship between black printer characteristics, prepress operator preferences, and color and spatial image quality. It would be worthwhile to have a better understanding of the theoretical basis of experiential practices used by prepress operators. This is particularly important if conventional systems are to be replaced with colorimetric systems. ▲

Acknowledgments. The authors thank T. Sanada and T. Uchida of Toppan Printing Co., America, Inc., for preparing the color proofing samples and K. Sate from the Multimedia Division of Toppan Printing Co., Ltd., who provided the conversion program from one four-dimensional image data-set to another four-dimensional image data-set, according to a color management module. Their help is greatly appreciated. This research was supported by Toppan Printing Co., Ltd.

Appendix: Characterization of a Desktop Drum Scanner for a Reflective Print Using the Spectral Kubelka–Munk Color Mixture Model

Spectral reflectance factor of the reflective material was reconstructed from scanned data using the Kubelka–Munk color mixture model for opaque materials.

Color Formation Theory of Reflective Photographic Material. The Kubelka–Munk theory² was selected as a model that can describe the relationship between the amount of dye in a material and its spectral reflectance factor for photographic-type color print paper. This is shown in Eq. A1,

$$R_\lambda = R_{\lambda,g} \exp[-2K_\lambda], \quad (A1)$$

$$K_\lambda = c_c k_{\lambda,c} + c_m k_{\lambda,m} + c_y k_{\lambda,y}, \quad (A2)$$

where K_λ is the spectral absorptance of the three dyes and $R_{\lambda,g}$ is the maximum spectral reflectance factor of the entire target. In addition, it was assumed that the additivity and proportionality laws were achieved in the absorptance space. Therefore, the spectral absorptance was described in Eq. A2. The analytical concentration of the cyan, magenta, and yellow dyes are given by c_c , c_m , and c_y . The unit spectral absorptivities, estimated using eigenvector analysis, are given by $k_{\lambda,c}$, $k_{\lambda,m}$, and $k_{\lambda,y}$.

Because of a refractive index discontinuity between air and the photographic paper, the Saunderson equations are used to convert between measured and internal reflectance.

$$R_\lambda = \frac{R'_\lambda - k_1}{1 - k_1 - k_2(1 - R'_\lambda)}, \quad (A3a)$$

$$R'_\lambda = k_1 \frac{(1 - k_1)(1 - k_2)R_\lambda}{1 - k_2 R_\lambda}, \quad (A3b)$$

where R_λ is the internal and R'_λ is the measured reflectance factor. Coefficient k_1 was set to 0.0 because the measurement instrument has 45/0 geometry. Coefficient k_2 was set to the theoretical value of 0.6.

The amount of dye in each color patch was determined by statistically estimating the dye concentrations, c_c , c_m , and c_y , using least squares minimization between measured and estimated spectral absorptance.

Relating Scanned Digital Counts to Reflectance Factor and Absorptance. Digital data obtained by scanning the input target must relate to the reflectance factor of the input target that corresponds to integrated dye concentration (absorptance) rather than analytical dye concentrations. However, the spectral responsivities of the scanner were unknown. Although the scanner has wideband and asymmetric spectral responsivities, it was assumed that the spectral responsivities were narrow band with a rectangular bandpass of 20 nm centered at 435, 545, and 645 nm. Therefore, it was assumed that the *B* channel relates to the average reflectance at 430 and 440 nm, the *G* channel relates to the average reflectance at 540 and 550 nm, and the *R* channel relates to the average reflectance at 640 and 650 nm. Using the gray-scale data, transformations for each channel from digital counts to these averaged reflectance factors were derived according to Eq. (A4),

$$r_i = \alpha_i \left(\frac{d_i}{2^8 - 1} \right)^{\gamma_i} + \beta_i, \quad (A4)$$

where r is the averaged narrow band reflectance factor, d is digital counts, and i represents each channel *R*, *G*, and *B*. Coefficients α_i , β_i , and γ_i are model coefficients. This function was selected because the scanner plug-in module uses a nonlinear LUT with gamma set to 1.8.

Using Eq. A4, scanned digital counts can be converted to quasi-reflectance r_R , r_G , and r_B . These quasi-reflectances were corrected by Saunderson's correction (Eq. A3a) and transformed to absorptance K_R , K_G , and K_B that correspond to the scanner responsivities according to the Kubelka–Munk theory, the inverse of Eq. A1, described

by Eq. A5. These absorptances express integral concentrations similar to the concept of integral densities. These integral concentrations must be converted to analytical concentrations to reconstruct the spectral absorptance of colors of the target. If responsivities of this scanner are similar to the narrow-band assumption, these transformations are performed by a linear transformation (a 3×3 matrix). This relation is shown in Eq. A6. Multilinear regression was used to predict the transformation coefficients, where concentrations were the dependent variables and integral concentrations from quasi-reflectances were the independent variables.

$$K_\lambda = \frac{\ln(R_\lambda / R_{\lambda, \max})}{-2.0} \quad (\text{A5})$$

$$\begin{pmatrix} c_c \\ c_m \\ c_y \end{pmatrix} = \begin{pmatrix} a_{1,1} & a_{1,2} & a_{1,3} \\ a_{2,1} & a_{2,2} & a_{2,3} \\ a_{3,1} & a_{3,2} & a_{3,3} \end{pmatrix} \begin{pmatrix} K_R \\ K_G \\ K_B \end{pmatrix}. \quad (\text{A6})$$

If responsivities of the scanner are far from the assumption, a second nonlinear relationship (a 3×11 matrix) was expected to account for the wideband spectral properties of the scanner. Linear, squared, and linear covariance terms were considered. This transformation is shown in Eq. A7.

$$\begin{pmatrix} c_c \\ c_m \\ c_y \end{pmatrix} = \begin{pmatrix} a_{1,1} & a_{1,2} & \cdots & a_{1,3} \\ a_{2,1} & a_{2,2} & \cdots & a_{2,3} \\ a_{3,1} & a_{3,2} & \cdots & a_{3,3} \end{pmatrix} \begin{pmatrix} K_R \\ K_G \\ K_B \\ K_R K_G \\ K_R K_B \\ K_G K_B \\ K_R K_G K_B \\ K_R^2 \\ K_R^2 \\ K_R^2 \\ 1 \end{pmatrix}. \quad (\text{A7})$$

Stepwise multi-linear regression was performed to determine transformation coefficients. Several terms were not statistically significant.

Transformation. The data flow to predict the spectral reflectance factor of a target color is: (1) Obtain scanner digital counts d_R , d_G , and d_B , (2) transform to quasi-reflectances r_R , r_G , and r_B using Eq. A4; (3) correct quasi-reflectances according to Saunderson's equation (A3a); (4) calculate quasi-absorptances K_R , K_G , and K_B (Eq. A5); (5) predict analytical concentration c_c , c_m , and c_y using a 3×3

(Eq. A6) or 3×11 (Eq. A7) matrix; (6) reconstruct spectral absorptance K_λ using dye absorptivities and Eq. A2, (7) transform to spectral reflectance factor R_λ from K_λ using Eq. A1 and $R_{\lambda, g}$; (8) compensate for reflective index discontinuity using the Saunderson correction of Eq. A3b; (9) finally, spectral reflectance factor R_λ' is predicted.

References

1. K. Iino and R. S. Berns, "Building color management modules using linear optimization I. Desktop color system," *J. Imaging Sci. Technol.* **42**, 79 (1998).
2. R. S. Berns, "Spectral modeling of a dye diffusion thermal transfer printer," *J. Electronic Imaging*, **2**, 359 (1993).
3. C. Nakamura and K. Sayanagi, "Gray component replacement by the Neugebauer equations," in *Neugebauer Memorial Seminar on Color Reproduction, Proc. SPIE* **1184**, 50 (1989).
4. P. Hung, "A smooth colorimetric calibration technique utilizing the entire color gamut of CMYK printers," in *Color Hard Copy and Graphic Arts III, Proc. SPIE* **2171**, 275 (1994).
5. P. Hung, "Smooth colorimetric calibration technique utilizing the entire color gamut of CMYK printers," *J. Electronic Imaging* **3**, 415 (1994).
6. S. Kita and H. Ogatsu, "L*a*b* based flexible UCR for both text and continuous images," *Display and Imaging* **2**, 33 (1993).
7. M. Tsukada and J. Tajima, "New algorithm for UCR using direct color mapping," in *Color Hard Copy and Graphic Arts IV, Proc. SPIE* **2413**, 365 (1995).
8. H. R. Kang, "Gray component replacement using color mixing models," in *Color Hard Copy and Graphic Arts III, Proc. SPIE* **2171**, 287 (1994).
9. "Toppan shows CMS it uses in-house," in *Color Management and Matching, The Seybold Report on Publishing Systems* **24**(21), 7 (1995).
10. W. F. Schreiber, "A color prepress system using appearance variables," *J. Imaging Technol.* **12**, 200 (1986).
11. R. Buckley, "A short history of device-independent color," in *Proc. IS&T and SID's Color Imaging Conference: Transforms & Transportability of Color*, 88 (1993).
12. American Society for Testing and Materials, *Standard test method for computing the colors of objects by using the CIE system*, ASTM Designation: E 308-90, Philadelphia, Pennsylvania, 1990.
13. J. A. C. Yule, *Principle of Color Reproduction*, John Wiley & Sons, New York, 1967.
14. I. Pobboravsky and M. Pearson, "Computation of dot areas required to match a colorimetrically specified color using the modified Neugebauer equations," in *Proc. 1972 of Technical Assoc. Graphics Arts*, 917 (1972).
15. H. E. J. Neugebauer, "Die theoretischen Grundlagen des mehrfarbendrucks," *Z. Wiss. Photog.* **36**(4) 73 (1937).
16. L. Wilkinson, *SYSTAT: The System for Statistics*, SYSTAT, Inc. Evanston, IL, 1989.
17. J. A. Yule and W. I. Nielsen, "The penetration of light into paper and its effect on halftone reproduction," *Proc. TAGA*, 65 (1951).
18. J. R. Huntsman, "A new model of dot gain and its application to a multi layer color proof," *J. Imaging Technol.* **13**, 136 (1987).
19. P. G. Engeldrum, "The color between the dots," *J. Imaging Sci. Technol.* **38**, 545 (1994).
20. J. Arney, P. G. Engeldrum and H. Zeng, "An expanded Murray-Davies model of tone reproduction in halftone imaging," *J. Imaging Sci. Technol.* **39**, 502 (1995).
21. J. Arney, C. D. Arney and P. G. Engeldrum, "Modeling the Yule-Nielsen halftone effect," *J. Imaging Sci. Technol.* **40**, 233 (1996).
22. R. K. Molla, *Electronic Color Separation*, R. K. Printing & Publishing Company, Charleston, West Virginia, 1988.
23. M. Southworth and D. Southworth, *Color Separation on the Desktop*, Graphic Arts Publishing, New York, 1993, p. 54.
24. R. S. Berns and M. J. Shyu, "Colorimetric characterization of a desktop drum scanner using a spectral model," *J. Electron. Imaging* **4**(4), 360 (1995).
25. J. Taft and N. Moroney, *Documentation for RITRC 30 LUT Version 1.0 for Alpha Release*, RIT Research Corporation, Rochester, NY (1994).